Heterogeneous activation of peroxymonosulfate by LaFeO₃ for diclofenac degradation: DFT-assisted mechanistic study and degradation pathways

YongFang Rao[a,e,*], Yufei Zhang[b,c], Fuman Han[a], Huichao Guo[a], Yu Huang[b,c], Ruoyu Li[d], Fei Qi[d], Jun Ma[e,*]

[a] Department of Environmental Science and Engineering, Xi'an Jiaotong University, Xi'an 710049, PR China
[b] Key Laboratory of Aerosol Chemistry and Physics, Institute of Earth Environment, Chinese Academy of Sciences, Xi'an 710075, PR China
[c] State Key Lab of Loess and Quaternary Geology (SKLLQG), Institute of Earth Environment, Chinese Academy of Sciences, Xi'an 710075, PR China
[d] College of Environmental Science and Engineering, Beijing Forestry University, Beijing 100083, PR China
[e] State Key Laboratory of Urban Water Resource and Environment, Harbin Institute of Technology, Harbin 150090, PR China

HIGHLIGHTS

- The highly efficient LaFeO₃ perovskite oxides were synthesized.
- DFT calculations are conducted for PMS adsorption and electron transfer.
- ATR-FTIR was used for in situ characterization of LFO surface during catalytic reaction.
- Activation mechanisms of PMS by LFO were proposed.
- Diclofenac degradation pathways were presented.

GRAPHICAL ABSTRACT
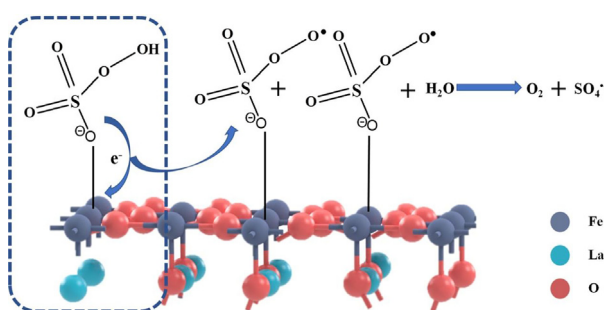
ABSTRACT

A perovskite oxide, LaFeO₃ (LFO), was synthesized and evaluated as a heterogeneous catalyst to activate peroxymonosulfate (PMS) for the oxidative degradation of diclofenac (DCF), a non-steroidal anti-inflammatory drug. It was observed that the catalytic activity of LFO was much higher than that of Fe₂O₃. LFO catalyzed PMS to degrade DCF with a turnover frequency ($2.02 \times 10^{-3} \, min^{-1}$) which is 17-fold higher than that of Fe₂O₃. Both sulfate and hydroxyl radicals were identified during LFO-activated PMS process by electron spin resonance (ESR). Radical competitive reactions indicate sulfate radicals played a major role in DCF degradation by LFO/PMS process. The PMS decomposition can be attributed to the formation of an inner-sphere complexation between the Fe (III) sites on LFO surface and PMS. Theoretical calculations illustrated the strong interaction between PMS and Fe (III) and electron transfer from PMS to Fe (III). Hydrogen temperature-programmed reduction (H₂-TPR) indicates that the LFO perovskite oxide is capable of facilitating an easier reduction of Fe (III) to mediate a redox process. Oxygen temperature-programmed desorption (O₂-TPD) suggests much more oxygen vacancies exist in LFO than in Fe₂O₃. Oxygen vacancies are favorable for the formation of chemical bond between Fe (III) and PMS and the activation of PMS. In situ ATR-FTIR analysis of LFO surface during PMS decomposition implies Fe (III)–Fe(II)–Fe (III) redox cycle was believed to account for the generation of sulfate radical. The intermediates generated during DCF degradation were identified and the possible degradation pathways were advanced in LFO/PMS system.

* Corresponding authors at: Department of Environmental Science and Engineering, Xi'an Jiaotong University, Xi'an 710049, PR China (Y. Rao).
E-mail addresses: yfrao@mail.xjtu.edu.cn (Y. Rao), majun@hit.edu.cn (J. Ma).

1. Introduction

Ubiquitously have pharmaceuticals been found in various waters due to their rising consumption and improper disposal [1,2]. The widespread occurrence of pharmaceuticals and their bioactive metabolites in the environment has incurred considerable environment, health and safety concerns in recent years [3,4]. Sewage treatment plants have been considered as the major source of the release of pharmaceuticals into the environment since they can survive conventional treatment systems [5,6].

Diclofenac (DCF), an important arylacetic acid non-steroidal anti-inflammatory drug (NSAID), is one of the most repeatedly detected pharmaceuticals in water environment due to its worldwide consumption and inefficient removal (21–40%) in wastewater treatment plants [2]. Exposure to DCF at environmentally relevant concentrations was reported to affect gill integrity, pituitary gene expression in fish [7,8], as well as hepatic and gonadal antioxidant defenses in fish [9]. DCF was also observed to induce embryotoxicity and teratogenesis in frog [10]. Such findings stimulate the need of integrating advanced technologies into conventional wastewater treatment.

Advanced oxidation processes (AOPs) have been proven to be a promising technology in the treatment of water and wastewater containing persistent organic pollutants (POPs) due to the generation of highly reactive radicals. Several AOPs including Fenton oxidation [11], photocatalysis [12], pulse radiolysis [13], ozonation [14], sonication [15] and photoelectrocatalysis [16], have been examined for DCF removal. In recent years, sulfate radicals have spawned evergrowing interests as a substitute of hydroxyl radical for the degradation of POPs. The generation of sulfate radical relies on the activation of peroxydisulfate (PDS) and peroxymonosulfate (PMS) by heat, UV, microwave and Ultrasound irradiation. The application of these sulfate radical-based processes in water treatment, however, has been curbed by the high energy demand. PMS and PDS can also be activated by transition metal ions, among which Co^{2+} was found to be the most effective activator for PMS to generate sulfate radical [17]. However, cobalt was identified as a possible human carcinogen by International Agency for Research on Cancer (IARC) [18]. Thus, the catalytic activity of varied cobalt oxides has also been evaluated as the activator of PMS [19–21]. Although these catalysts have been proven effective in inducing the generation of sulfate radicals, they still entail a health risk due to the cobalt ions leaching from the solid phase. Seeking alternative metal oxides as efficient and stable activators for PMS still remains a challenge for the practical application of this technology.

Perovskite oxides, with the general formula of ABO_3 (or A_2BO_4), have attracted increasing interests as an important functional materials, due to the flexible chemical composition, element abundance and structural stability. Some studies on perovskite-type oxides (PTOs) as catalysts to activate PMS or H_2O_2 have been reported [22–30], most of which centered on the activation of PMS by cobalt based-perovskite catalysts. The investigation on the heterogeneous activation of PMS by iron-based PTOs is limited. The mechanisms underlying PTOs-activated PMS reaction are far from being completely understood.

Thus, this work sets out to evaluate the applicability of perovskite for DCF degradation by activating PMS. $LaFeO_3$ (LFO), as an iron-containing perovskite-type oxide, was synthesized by a sol-gel procedure. The morphology, textural property, and crystalline structure of as-synthesized LFO nanoparticles were systematically characterized by varied techniques. The catalytic activity of $LaFeO_3$ was evaluated in terms of the degradation rates of DCF. The effects of dissolved oxygen, ion strength and radical scavengers were investigated on the degradation of DCF. The reaction mechanisms underlying LFO-activated PMS process were illuminated. The intermediates/products were identified and the possible decay pathways were proposed.

2. Materials and methods

2.1. Materials

Lanthanum nitrate hexahydrate ($La(NO_3)_3$ $6H_2O$), iron nitrate nonahydrate ($Fe(NO_3)_3$ $9H_2O$), citric acid monohydrate ($C_6H_8O_7$ H_2O), bismuth nitrate pentahydrate ($Bi(NO_3)_3$ $5H_2O$), sodium tetraborate and nitrobenzene (NB) were obtained from Sinopharm Chemical Reagent Co., Ltd, China. Diclofenac (2-[2,6-dichlorophenyl]-amino]-benzene acetic acid sodium salt), 2, 6-dichloroaniline, Oxone and La_2O_3 were purchased from Sigma-Aldrich, with the highest purity. All organic solvents were HPLC grade. All aqueous solutions were prepared in distilled and deionized water (DDW).

2.2. Catalyst synthesis

The perovskite LFO was prepared with a sol-gel method. Lanthanum nitrate, ferric nitrate, and citric acid were added into 30 mL DDW in a molar ratio of 1:1:2. The resulting brown solution was stirred for 24 h and then heated for 12 h in water bath at 80 °C. The obtained sticky gel was dried under vacuum. The sticky gel was calcined for 4 h in a muffle furnace (5K/min) at 500 °C. After being calcined, the sample was subjected to ball-grinding, washed several times with ethanol and Milli-Q water, and dried overnight at 105 °C. Fe_2O_3 was synthesized following the same procedure. $BiFeO_3$ were synthesized by a microwave assisted hydrothermal method. Bismuth nitrate and ferric nitrate were dosed into DDW with a molar ratio of 1:1. The mixture was stirred for 1 h as the precursor of $BiFeO_3$. The precursor solution was stirred for 0.5 h after the addition of sodium carbonate (Na_2CO_3) and potassium hydroxide (KOH) as mineralizers. The obtained solution was heated in a 500 W microwave oven with the frequency of 2450 Hz at constant temperature (140 °C) for 35 min. After being cooled down, the particles were washed several times with Milli-Q water and dried at 80 °C for 12 h. The resulting product was finally grinded into fine powders.

2.3. Catalyst characterization

The crystal structures of as-prepared catalysts were determined by X-ray powder diffraction (XRD) at a scan rate of $0.05°\,min^{-1}$ (PANalytical Corp., The Netherlands). The morphology of as-prepared $LaFeO_3$ was characterized by TEM performed on the JEOL 2010 instrument (JEOL Corp., Japan), respectively. The surface chemical composition and chemical state of catalyst was analyzed by analyzed by the X-ray photoelectron spectroscopy (AXIS ULtrabld, Kratos). The C 1 s at 284.8 eV was adopted for the correction of spectra in XPS analysis. The Brunauer–Emmett–Teller (BET) surface area and pore structure of the catalysts were obtained from N_2 adsorption/desorption isotherms at 77 K using an ASAP 2020 automatic analyzer (Micromeritics Instrument Corp., Norcross, GA, USA).

The temperature-programmed reduction by hydrogen (H_2-TPR) was conducted with autoadsorption apparatus (Builder PCA-1200, Beijing Builder Co. Ltd, China) with a thermal conductivity detector. 50 mg of each catalyst was pretreated in nitrogen at 573 K for 1 h. After cooling to room temperature, H_2-TPR was recorded in an H_2 flow (5 vol% H_2 in Ar) of 30 mL/min with a constant heating rate of 10 K/min and final temperature of 1073 K. For O_2-TPD, 50 mg of sample were heated from room temperature to 300 °C at a rate of 10 K/min and held for 30 min. After being cooled down to room temperature, the catalyst was purged by a stream of O_2 (30 mL/min) for 1 h. Then, the sample was heated up to 800 °C at a rate of 10 K/min with the purging of nitrogen (30 mL/min).

The Zeta potentials of samples were acquired on a Malvern Zetasizer Nano ZS90. To identify the radicals generated in LFO/PMS, electron spin resonance (ESR,) measurements were conducted (Bruker EMXPLUS6/1) using DMPO (5, 5-dimethyl-pyrroline N-oxide) as the spin trapping agent.

2.4. ATR-FTIR analysis

A Bruker FTIR spectrometer (Tensor II) equipped with a Universal ATR accessory was used to determine the changes of the LFO surface in presence of PMS in water. Deionized water was scanned as background. Spectra of the samples were automatically subtracted by the water spectrum during the scans. 50 mg of LFO particles were suspended in 10 mL of deionized water (pH 6.5) or PMS solution (2.5 mM; pH 6.5) in glass tubes before analysis. The suspension was dropped on the ZnSe crystal of the ATR accessory with an autopipette and scanned times in the range of 800–4000 cm^{-1} at a resolution of 4 cm^{-1}.

2.4.1. Batch reaction

The degradation experiments were conducted in 250 mL glass beakers. The specific aliquots of DCF stock solution (0.2 mM) were added into the DDW to obtain a final volume of 100 mL. The as-prepared LFO or other catalysts were added into DCF solution and sonicated for 5 min (No DCF degradation was observed during 5 min sonication). The reactions were initiated by the addition of PMS stock solution into the reactor. Tetra-borate was used as a buffer to control pH level. Samples withdrawn at a predetermined time interval were filtered through a Millipore PTFE membrane with 0.2 μm pore size and quenched by sodium thiosulfate prior to quantification by High Performance Liquid Chromatography (HPLC). All experiments were carried out in duplicate and the error bars showed the standard deviation of the replicate experimental data.

2.5. Analytic methods

The residual DCF after reaction was determined by HPLC. The concentration of the remaining PMS during the reaction was determined by an iodometric method [31]. In addition, possible cation leaching (La and Fe) was monitored by means of ICP (Inductively coupled plasma) (ICPE-9000, SHIMADZU).

Liquid chromatography/electrospray-time-of-flight mass spectrometry (LC/ESI-TOF-MS), were used to identify the intermediates generated during diclofenac degradation. Separation was conducted by Agilent HPLC system (1290 Autosampler, 1290 Bin Pump and 1290 DAD) equipped with a reverse-phase 2.1 mm × 150 mm C18 analytical column and 1.8 μm particle size (Agilent Eclipse Plus C18). SPME (Solid phase microextraction)/GC/MS was also used to identify the degradation intermediates. The detailed procedure was described in our previous study [32].

The generation of low molecular weight acids were detected and quantified by the ion chromatograph (Dionex IC-1500) composed of an anion column (Dionex IonPac AS19, 4 mm × 250 mm), a guard column (Dionex Ionpac AG19, 4 mm × 50 mm) and Dionex DS6 conductivity detector. A KOH solution was used as the mobile phase eluting at 1 mL/min. Gradient elution was 1 mM KOH for 5 min, followed by a linear enhancement to 35 mM in 28 min, and then back to 1 mM in 5 min.

Total organic carbon (TOC) concentration was measured by a TOC analyzer (Shimadzu TOC-L CPN).

The DFT (density functional theory) calculations were conducted using the program CASTEP package [33]. The detailed calculation method was the same as described in our previous studies [34–36] except a plane-wave cutoff of 400 eV and a 4 × 3 × 4 Monkhorst-pack *k*-point mesh for the geometry optimization.
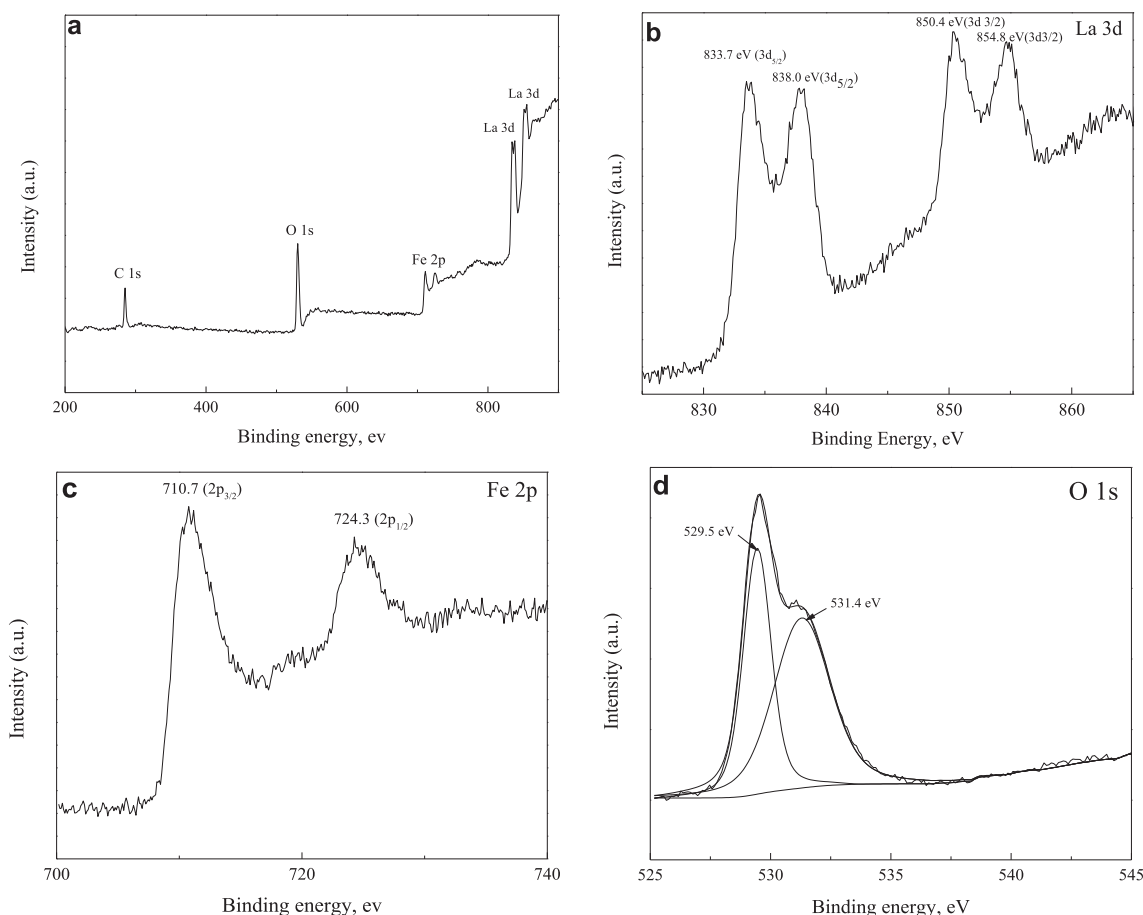

Fig. 1. XPS spectra of as-prepared LFO: (a) survey spectrum; (b) La 3d; (c) Fe 2p and (d) O 1s.

3. Results and discussion

3.1. XRD characterizations and surface chemical states of as-prepared LFO

The XRD pattern of as-synthesized LFO was shown in Fig. S1. The peaks located at 22.6°, 32.2°, 39.7°, 46.2°, 57.5°, 67.5° and 76.6° could be ascribed to the characteristic diffraction peaks of 101, 121, 220, 202, 123, 242 and 204 planes of LFO (PDF No. 88-641), suggesting the formation of phase-pure LFO crystallized with orthorhombic structure. The average crystallite size of as-prepared LFO is about 18.4 nm, as estimated from the strongest 121 diffraction peak by Scherrer Equation.

To identify the surface chemical states and composition of the as-prepared LFO samples, the synthesized LFO was characterized by XPS. Fig. 1 presents the survey spectrum and high-resolution spectra of La 3d, Fe 2p and O 1s orbitals. The survey spectrum confirmed the presence of La, Fe, and O elements. In the spectrum of La 3d (See Fig. 1b), the peaks at 833.7 eV and 838.0 eV correspond to $3d_{5/2}$ orbital of La^{3+} while the peaks of La $3d_{3/2}$ locate at 850.4 eV and 854.8 eV. The double contribution suggests the presence of La^{3+} in different surface environment, namely La^{3+} in the LFO perovskite structure (833.7 eV) and La^{3+} in $La(OH)_3$ (838.0 eV). The two peaks at binding energies of 710.7 and 724.3 eV are characteristics of the Fe (III) (See Fig. 1c). Moreover, the asymmetric shape of O 1s peak, which can be deconvolved into two separate peaks at 529.4 and 531.3 eV (Fig. 1d), suggests that the lattice oxygen and hydrogen bonded oxygen (O − H) are both present on the surface.

3.2. Morphology and textural property of as-prepared LFO

In order to understand the morphology and crystalline structure of as-prepared LFO, TEM characterization was conducted. Fig. 2a–d displays typical TEM, high-resolution TEM (HRTEM) and SAED (Selected area electron diffraction) patterns of LFO sample. As demonstrated in Fig. 2a, strong contrast view in the image shows that LFO was formed in an irregularly circular pattern, suggesting the formation of LFO sphere. The dimension of LFO was estimated to be around 20 nm from Fig. 2a, which accords with XRD calculation result. The HRTEM images in Fig. 2b and 2c display lattice fringes with d-spacings of ca. 0.27 and 0.39 nm, which correspond well to the (1 2 1) and (1 0 1) planes of the orthorhombic-structured LFO, respectively. Multidiffraction rings indicate as-prepared LFO is polycrystalline as observed in Fig. 2d.

The BET specific surface area, pore-size distribution, and pore volume for as-prepared LFO were examined by their N_2 adsorption/desorption isotherms to evaluate their potential as catalytic materials (See Fig. S2). The shape of the physisorption isotherm is in accordance with type IV with a type H3 hysteresis loop in the P/P_0 range of 0.7–1.0, and this is the typical characteristic of mesopores, according to IUPAC classification. The BET specific surface area, pore volume and average pore diameter of LFO is $27.4 \, m^2/g$, $0.244 \, cm^3/g$ and 35.6 nm, respectively.

3.3. Catalytic activity and stability of the perovskite LFO

Fig. 3 shows DCF degradation in sole-catalyst, sole-PMS solution and PMS combined with LFO, $BiFeO_3$, La_2O_3, and Fe_2O_3, respectively.
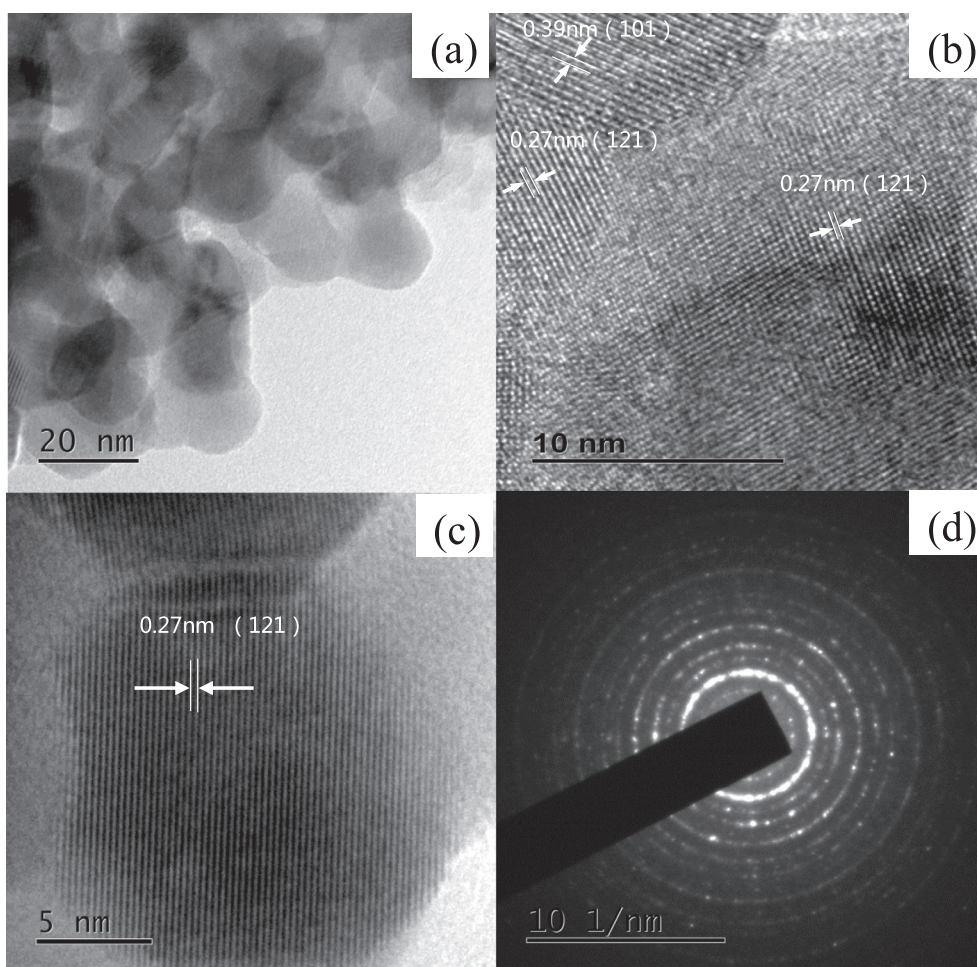

Fig. 2. (a) Low-magnification TEM image of LFO; (b) and (c) high-resolution TEM image of LFO; (d) SAED image of LFO.
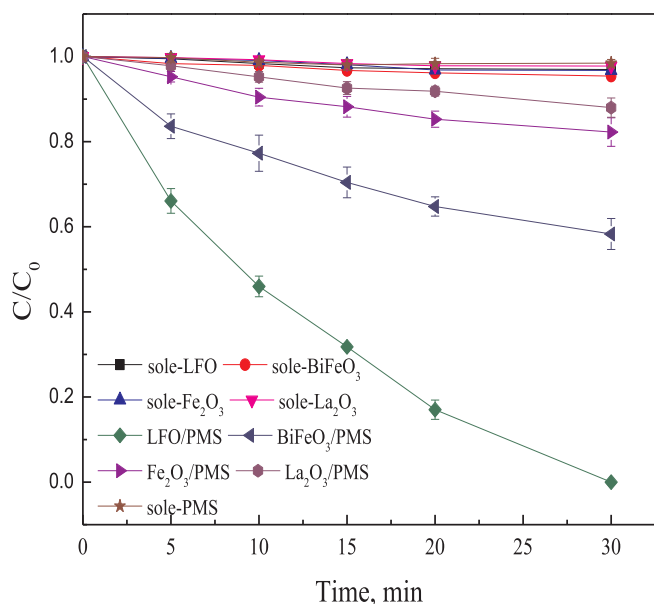
Fig. 3. DCF degradation in sole-catalyst, sole-PMS and catalytic PMS systems. (Notes: Oxide dosage = 0.1 g/L, $[DCF]_0$ = 0.025 mM, $[PMS]_0$ = 0.5 mM, tetraborate buffered pH 7.0).

Fe_2O_3 and $BiFeO_3$ were utilized to evaluate the catalytic activity of Fe (III) in non perovskite and perovskite crystals. The XRD patterns of Fe_2O_3 and $BiFeO_3$ are shown in Fig. S3. The BET specific surface area of the synthesized $BiFeO_3$ and Fe_2O_3 was measured to be 2.544 m^2/g and 11.6 m^2/g by their N_2 adsorption/desorption isotherms, respectively. The possible activity of La (III) was assessed using La_2O_3 as a catalyst. As illustrated in Fig. 3, nearly no DCF removal was observed in sole-PMS system. No DCF degradation was observed in the suspension of all catalysts without the addition of PMS and the adsorption of DCF on the catalysts was insignificant (less than 5%). It was also noticed that DCF concentration decline was insignificant in La_2O_3/PMS system. Around 18% of DCF removal efficiency was achieved in Fe_2O_3/PMS. A rapid DCF degradation was observed in $BiFeO_3$/PMS system and was even faster in LFO/PMS system (100% removal). The adsorption of DCF on the surface of La_2O_3, Fe_2O_3 and LFO is unimportant (less than 5%). These results indicate Fe (III) might be the active metal site of LFO, which needs to be further confirmed. The turnover frequency (TOF) per active site is considered as an important factor to evaluate the activity of the catalysts, based on the assumption that every iron atom is catalytically active. LFO catalyzed PMS to degrade DCF with a TOF (2.02×10^{-3} min^{-1}) which is approximately 17-fold higher than that of Fe_2O_3. DCF degradation was found to follow pseudo-first-order kinetics in heterogeneous activation of PMS by different catalysts as shown in Fig. S4.

To examine the stability of LFO as an activator of PMS, the LFO particles were recovered and recycled for 4 times. The DCF degradation rate kept almost constant in PMS/LFO system, as shown in Fig. S5. The spectra of La 3d, Fe 2p and O 1s orbitals were compared between fresh LFO and spent LFO after 2 cycles of reaction. As illustrated in Fig. S6, no obvious change was observed. The concentration of iron leaching from LFO to solution during 30 min reaction is below the detection limit of iron by ICP. The low iron leaching of LFO further confirmed its stability of LFO during the repeated reactions. The high stability and catalytic activity render LFO a promising catalyst for the activation of PMS in practical application.

3.4. Influence of ionic Strength, radical scavengers and identification of reactive radicals

The increment of ionic strength appreciably interferes with outer-sphere interactions such as electrostatic bonding between the solute and the surface of colloidal particle while inner-sphere complexation is not influenced [37]. As demonstrated in Fig. 4a, DCF degradation was not inhibited with the addition of $NaClO_4$, which was utilized to regulate the ionic strength of the reaction solution. This result suggests a strong inner-sphere interaction exists between the PMS ions and the active metal sites on the crystalline facet of LFO [38]. Namely, covalent binding or complexation between PMS ions and the active metal sites initiated the activation of PMS. The promoting effect of ClO_4^- was also observed in the degradation of bisphenol A using a $CuFe_2O_4$/PMS process [39].

Both hydroxyl radical and sulfate radical may contribute to the degradation of organic pollutants by activated PMS process. Tert-butanol (t-BuOH) is an effective scavenger for hydroxyl radical ($k_{OH} = (3.8–7.6) \times 10^8$ $M^{-1}s^{-1}$) but not for sulfate radical ($k_{SO4} = (4–9.1) \times 10^5$ $M^{-1}s^{-1}$) [40]. Methanol can capture both hydroxyl radical ($4.6–9.7 \times 10^8$ $M^{-1}s^{-1}$) [41] and sulfate radical ($1.1–2.5 \times 10^7$ $M^{-1}s^{-1}$) [40] very rapidly. Therefore, these two radical capturers were applied to determine the contribution of these two radicals in DCF degradation. The two scavengers were observed to exert no significant effect on HSO_5^- degradation (Fig. S7). As shown in Fig. 4b, the presence of 0.1 M t-BuOH decreased DCF degradation rate constant from 0.0833 to 0.0616 min^{-1} after 30 min of reaction, and DCF decay rate constant decreased from 0.0833 to 0.0512 min^{-1} in the presence of 0.1 M Methanol. Even with 1.0 M methanol present in the reaction solution, around 72% DCF removal was achieved and DCF degradation rate constant was 0.424 min^{-1}. In order to further probe the role of the two radicals, HCO_3^- was used as inorganic radical scavengers. Both hydroxyl radical and sulfate radicals react fastly with HCO_3^- ($k_{OH} = 8.5 \times 10^6$ $M^{-1}s^{-1}$, $k_{SO4} = 1.6 \times 10^6$ $M^{-1}s^{-1}$) [42]. As also illustrated in Fig. 4b, significantly was DCF degradation inhibited in the presence of 10 mM HCO_3^-, DCF degradation rate constant declining from 0.0833 to 0.013 min^{-1}. This result might imply DCF degradation relied on the oxidation of hydroxyl radicals or sulfate radicals. However, the presence of HCO_3^- also considerably retarded the decomposition of PMS as shown in Fig. S7. The inhibiting effects of HCO_3^- can be rationalized as follows: LFO particles were positively charged at pH 7.0 ± 0.5, which favored HCO_3^- approaching the surface and forming inner-sphere complexes with the active metal sites [43], leaving less active metal sites available to initiate HSO_5^- decomposition on LFO surface. NB is susceptible to HO· oxidation with a reaction rate constant of 3.9×10^9 $M^{-1}s^{-1}$ [41], whereas it exhibits low reactivity towards sulfate radical ($< 10^6$ $M^{-1}s^{-1}$) [44]. Thus, DCF degradation was examined in the presence of NB. The insignificant inhibiting effect of NB (Fig. S8) implies sulfate radical made a major contribution to DCF degradation in LFO/PMS system. Metal oxides have a strong adsorption ability for hydroxyl radicals due to their hydrophilicity [45] since there are many hydroxyl groups on the LFO surface (See Fig. 1d). Only a small part of hydroxyl radicals and sulfate radicals may escape from LFO surface and diffuse into bulk solution. On the other side, methanol and t-BuOH mainly capture the radicals in the bulk solution. Thus, these two radical scavengers failed to inhibit DCF degradation significantly. The results indicate DCF was oxidized primarily by the radicals adsorbed on the surface of LFO. Similar phenomena were also reported in a previous study [39]. The 2-propanol was reported to react with both free and adsorbed hydroxyl radicals [46]. Fig. 4b shows 2-propanol exhibited more significant inhibiting effect on DCF degradation than methanol did. However, 0.1 M 2-propanol could not completely inhibit DCF degradation, either. This may be because sulfate radicals made a major contribution to DCF degradation.

To corroborate the involvement of reactive radicals during DCF degradation by LFO/PMS process, the ESR technique was employed with DMPO as the spin trapping agent. As demonstrated in Fig. 4c, the typical DMPO·-OH and DMPO·-SO_4 signals verified the generation of hydroxyl and sulfate radicals in $LaFeO_3$/PMS system based on their

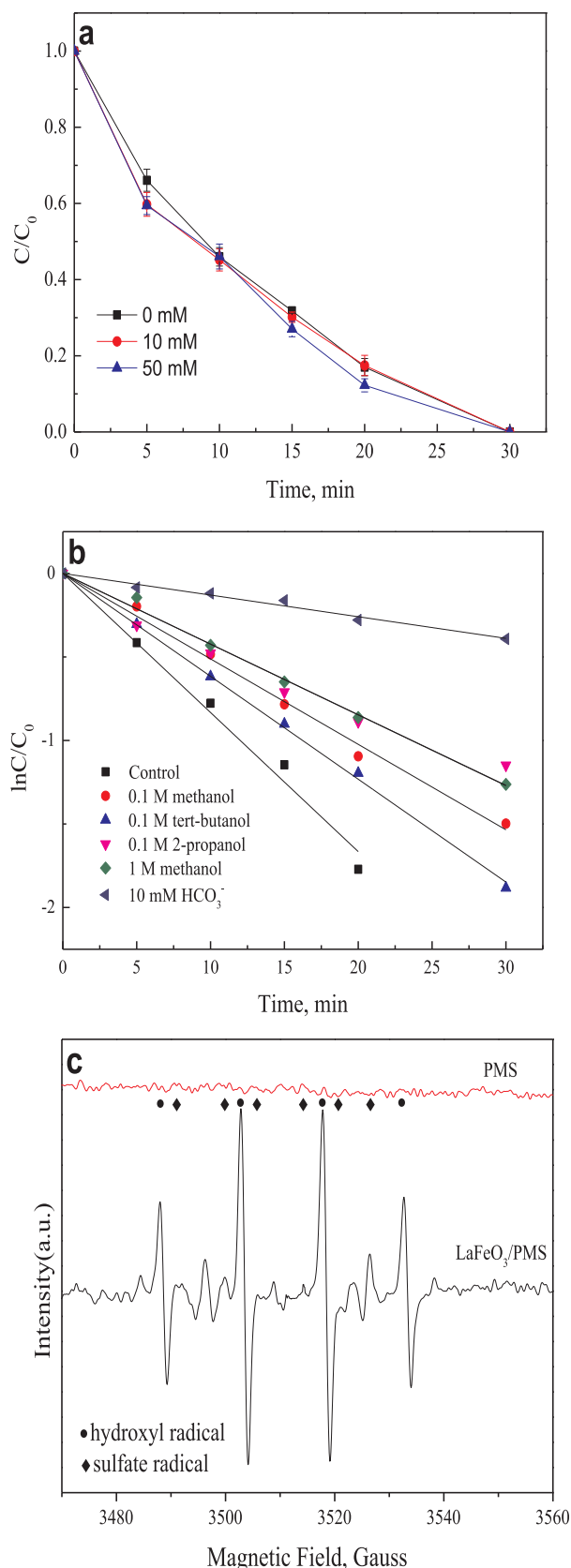**Fig. 4.** (a) Influence of ion strength on DCF degradation; (Notes: $[DCF]_0 = 0.025\,mM$, LFO dosage = 0.1 g/L, $[PMS]_0 = 0.5\,mM$, tetraborate buffered pH 7.0) (b) Influence of radical scavengers on DCF degradation rate; (Notes: $[DCF]_0 = 0.025\,mM$, LFO dosage = 0.1 g/L, $[PMS]_0 = 0.5\,mM$, tetraborate buffered pH 7.0) (c) DMPO spin-trapping ESR spectra of PMS and LFO/PMS.

hyperfine splitting constants (DMPO·-OH: $a_N = a_{\beta\text{-}H} = 14.9\,G$; DMPO·-SO$_4$: $a_N = 13.67\,G$, $a_{\beta\text{-}H} = 10.24\,G$, $a_{\gamma\text{-}H1} = 1.52\,G$, $a_{\gamma\text{-}H2} = 0.79\,G$) [47]. Although the insignificant influence of NB suggests the major role of sulfate radicals in DCF degradation, the fast hydrolysis of DMPO·-SO$_4$ adduct to DMPO·-OH adduct [48] resulted in the weak signal of DMPO·-SO$_4$. Mixing of 1 mM PMS and 88 mM DMPO could not form any signal.

3.5. DFT calculations

To further investigate the effect for PMS activation on the surface of LFO, density functional theory (DFT) calculations are performed for PMS adsorption on LFO (1 0 0) lattice plane. For adsorption on the LFO (1 0 0) lattice plane in Fig. 5a, PMS is chemisorbed on the LFO (1 0 0) surface with the one O atom on the –SO$_4$ side bonding with the Fe atom on the surface, suggesting the Fe atom is the active adsorption site of PMS on LFO (1 0 0) surface. The bond length of the three Fe–O bonds in the LFO (1 0 0) surface is 1.917 Å, 1.786 Å and 1.800 Å, respectively. The bond length of O–Fe between Fe and HSO$_5^-$ is 1.977 Å, implying the interaction between Fe and HSO$_5^-$ is neither too strong nor too weak, which favors the catalytic activity of LFO for PMS activation according to Sabatier's principle [49]. To better understand the activation of PMS on LFO surface, the charge carriers transfer between the LFO surface and PMS was examined. Fig. 5b provides the electron density difference (EDD) of LFO with PMS absorbed on the (1 0 0) lattice plane. The Miliken population analysis based on the EDD results demonstrates that about 0.3 electrons transfer from PMS to LFO on the surface, indicating that the Fe atom on the LFO (1 0 0) lattice plane is reduced.

3.6. Reducibility and oxygen species

The BET specific surface area of LFO (27.4 m^2/g) is larger than that of Fe$_2$O$_3$ (11.6 m^2/g). However, the amount of DCF adsorbed on LFO surface (around 3.1%) is similar to that adsorbed on Fe$_2$O$_3$ (3.3%). Thus, the larger BET specific surface area of LFO may not make a major contribution to its higher catalytic activity in comparison with Fe$_2$O$_3$. There are other factors which may contribute to the high catalytic activity of LFO.

The H$_2$-TPR experiments were conducted to determine the reduction properties of the catalysts. As shown in Fig. 6a, H2-TPR profile of Fe$_2$O$_3$ exhibited two reduction peaks at 409 and 633 °C, corresponding to the reduction of Fe$_2$O$_3$ to Fe$_3$O$_4$ and the reduction of Fe$_3$O$_4$ to FeO [50,51]. Fig. 6a also shows H$_2$ consumption started at a temperature of 301 °C over LFO, approximately 109 °C lower than that over Fe$_2$O$_3$, indicating the high-valence-state iron ions in LFO are easier to be reduced to a lower oxidation state than those in Fe$_2$O$_3$, i.e., iron ions in LFO are better electron acceptors for PMS than iron ions in Fe$_2$O$_3$. Since the electrons were transferred from PMS to LFO in the interaction between PMS and LFO on the basis of DFT calculation, LFO was supposed to be a better catalyst than Fe$_2$O$_3$ in terms of PMS activation. The reduction peaks located below 700 °C belong to the reduction of Fe^{3+} to Fe^{2+}. The reason why multiple peaks correspond to the reduction of Fe^{3+} to Fe^{2+} may be the different bond energy of Fe–O bonds on the surface of LFO on the basis of DFT calculations. The peak (> 700 °C) of LFO can be ascribed to the reduction of Fe^{2+} to Fe^0 [52].

The difference of oxygen species between Fe$_2$O$_3$ and LFO was investigated by O$_2$-TPD tests. As demonstrated in Fig. 6b, there is one O$_2$ desorption peak below 200 °C for both Fe$_2$O$_3$ and LFO, which corresponds to the surface adsorbed oxygen species such as O$_2^-$ or O$^-$. For both LFO and Fe$_2$O$_3$, there are two desorption peaks of oxygen which located between 300 and 500 °C, which are associated with the desorption of the oxygen chemically adsorbed on the oxygen vacancies or surface lattice oxygen [53,54]. The peak at 532 °C for LFO and the peak at 537 °C for Fe$_2$O$_3$ can be ascribed to the desorption of surface lattice oxygen [55]. The peaks above 600 °C come from the desorption of bulk
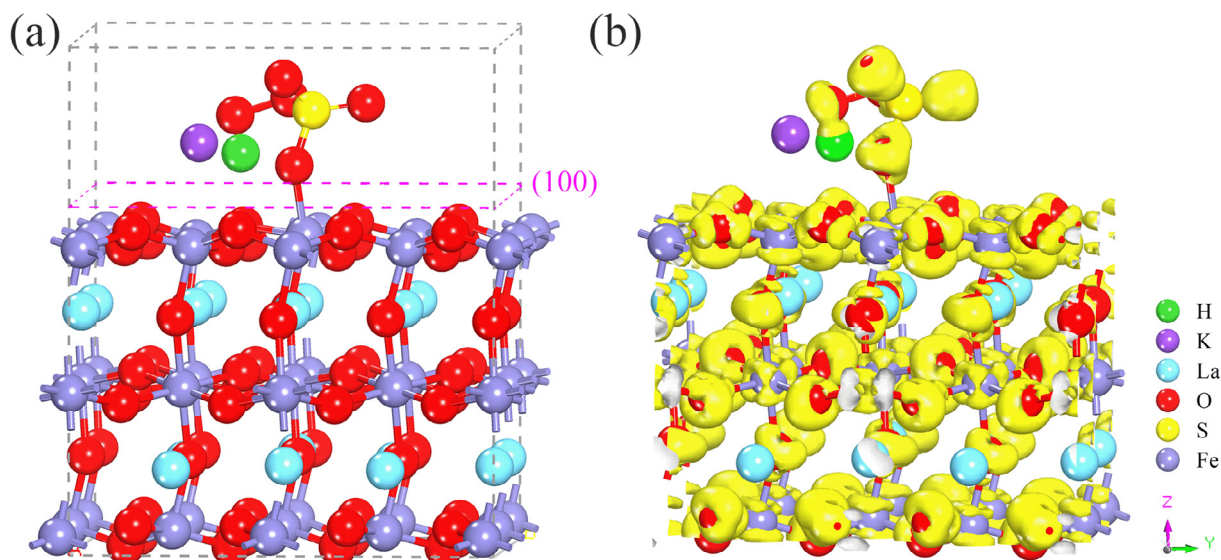
Fig. 5. (a) The crystal models after geometry optimization; (b) The calculated electron density difference (EDD) diagrams of LaFeO$_3$ with PMS absorbed in the (1 0 0) lattice plane. (Note: yellow area represents the increase of electron density).

lattice oxygen for both LFO and Fe$_2$O$_3$. The reason why multiple peaks correspond to the desorption of surface lattice oxygen may be the different bond energy of Fe–O bonds on the surface of LFO on the basis of DFT calculations. As also shown in Fig. 6b, the intensity of peaks between 300 and 600 °C for LFO is much stronger than that for Fe$_2$O$_3$, indicating much more oxygen vacancies and higher oxygen mobility on the surface of LFO than those on Fe$_2$O$_3$ surface. The oxygen vacancies could facilitate the formation of chemical bond between perovskite catalysts and PMS, and subsequently prop up the reactivity of transition metal ion towards PMS [56].
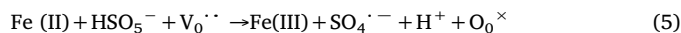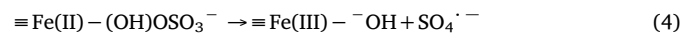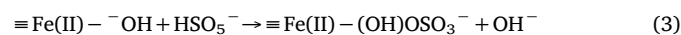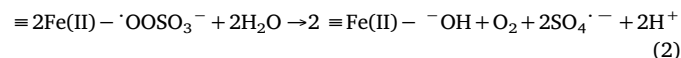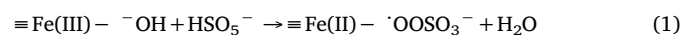
3.7. Reaction mechanisms of LaFeO$_3$-cctivated PMS

It is suggested that free Fe^{3+} ion can be reduced to Fe^{2+} by PMS [57]. It is not easy to directly identify the reduction of Fe^{3+} on the oxide surface during the interaction between HSO$_5^-$ and LFO. It is believed Fe^{2+} has larger ionic radii than Fe^{3+}, leading to a weaker binding capability with ligands. Thus, the binding capacity of surface hydroxyl groups, is supposed to vary with the valence state of iron. In order to clarify the interaction between PMS and LFO, the LFO surface was characterized by in situ ATR-FTIR during catalytic decomposition of PMS (Fig. 7). The two peaks at 1254 cm^{-1} and 1098 cm^{-1} in the IR spectra can be ascribed to the S–O stretching vibration of either HSO$_5^-$ or SO$_4^{2-}$.[58] The intensity of the peak at 1254 cm^{-1} obviously decreased in comparison with the adjacent peak (1093 cm^{-1}) in the presence of LFO, implying this peak results from the S–O stretch of HSO$_5^-$. In addition, there is 17 cm^{-1} red shift of this peak in the presence of LFO relative to the sole-PMS solution, indicating the S–O bond of HSO$_5^-$ was weakened when bonded to LFO surface. It may be because the surface Fe (III) accepted electron from HSO$_5^-$ leaving the S–O bond of PMS weaker.

Fig. 7 also shows ATR-FTIR spectra of LFO slurry with water spectrum as background. The peak at 3126 cm^{-1} is believed to come from the stretching vibration of surface –OH on LFO surface. In the presence of PMS, this peak blue-shifted by 74 cm^{-1}. The blue-shift of the surface –OH peak indicates the increase in the electron density of the surface –OH during the interaction between LFO and PMS. It can be rationalized by the decrease of electron-withdrawing capacity of the bonded Fe, which may be attributed to a lower transient valence of Fe. Consequently, the ATR-FTIR results indicate the existence of inner-sphere complexation and surface –OH groups were possibly bonded to a lower transient valence of Fe. These results are in accord with the conclusion

drawn from Fig. 4 and the conclusion that Fe (III) was reduced during the PMS-LFO interaction based on DFT calculation.

In this study, we observed the generation of small gas bubbles during the LFO-PMS interaction at high concentration (See Fig. S9), which was also documented by in the study of Zhang et al. involving the catalytic degradation of PMS by CuFe$_2$O$_4$.[38] It is reasonable to assume small gas bubbles were ascribed to the production of O$_2$. Thus, the mechanisms underlying LFO-activated PMS can be described in Eqs. (1–4). The Fe (III) on the surface of LFO oxidized HSO$_5^-$ to SO$_5^{\cdot -}$, and then adjacent SO$_5^{\cdot -}$ bonded on the LFO surface united with each other to generate O$_2$ and sulfate radicals. At the same time, Fe (III) was reduced to Fe (II) and the new surface –OH group was formed (Eq. (3)). The interaction between Fe (II)–OH and HSO$_5^-$ resulted in the formation of Fe (II)–(HO) OSO$_3^-$ complex (Eq. (3)), inside which the electron transfer led to the generation of sulfate radical. In addition, the presence of oxygen vacancies might also play a non-negligible role in the interaction between PMS and LFO, as described in Eq. (5).

$$\equiv Fe(III) - {}^-OH + HSO_5^- \rightarrow \equiv Fe(II) - {}^\cdot OOSO_3^- + H_2O \qquad (1)$$

$$\equiv 2Fe(II) - {}^\cdot OOSO_3^- + 2H_2O \rightarrow 2 \equiv Fe(II) - {}^-OH + O_2 + 2SO_4^{\cdot -} + 2H^+ \qquad (2)$$

$$\equiv Fe(II) - {}^-OH + HSO_5^- \rightarrow \equiv Fe(II) - (OH)OSO_3^- + OH^- \qquad (3)$$

$$\equiv Fe(II) - (OH)OSO_3^- \rightarrow \equiv Fe(III) - {}^-OH + SO_4^{\cdot -} \qquad (4)$$

$$Fe\ (II) + HSO_5^- + V_O^{\cdot\cdot} \rightarrow Fe(III) + SO_4^{\cdot -} + H^+ + O_O^\times \qquad (5)$$

where $V_O^{\cdot\cdot}$ represents a doubly charged oxygen vacancy in the bulk and/or on the surface of LFO and $O_O^\times$ is the oxygen ion locating where oxygen vacancy is. Thermodynamically, the reduction of Fe (III) by PMS is unfavorable due to higher redox potential of HSO$_5^-$ (1.8 V) than Fe (III) (0.77 V). However, the perovskite oxides can facilitate valence-state changes of the B-site cation without phase transition, which was proven by the H$_2$-TPR result. In addition, the pH$_{pzc}$ of Fe$_2$O$_3$ was determined to be around 5.2 (data not shown). At pH 7.0, Fe$_2$O$_3$ was negatively charged, preventing HSO$_5^-$ from approaching its surface.

3.8. Identification of DCF degradation intermediates and possible decay pathways

DCF degradation intermediates were identified by UPLC-TOF/ESI-MS in a positive ionization mode. SPME/GC/MS was also utilized to
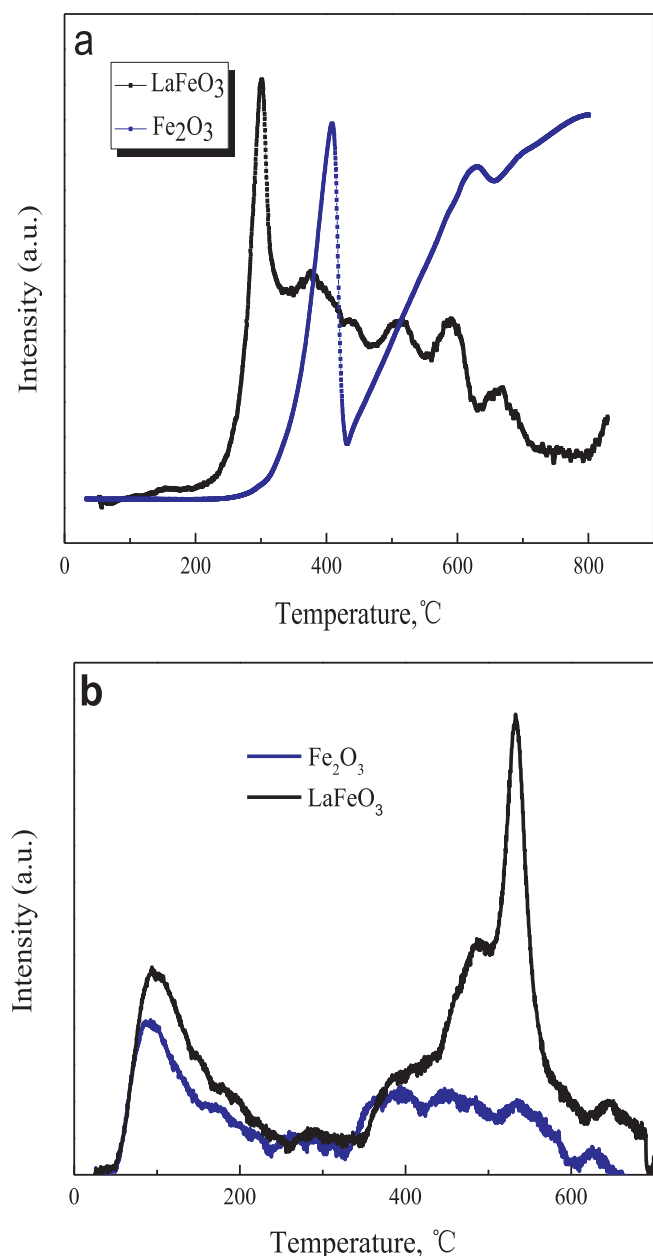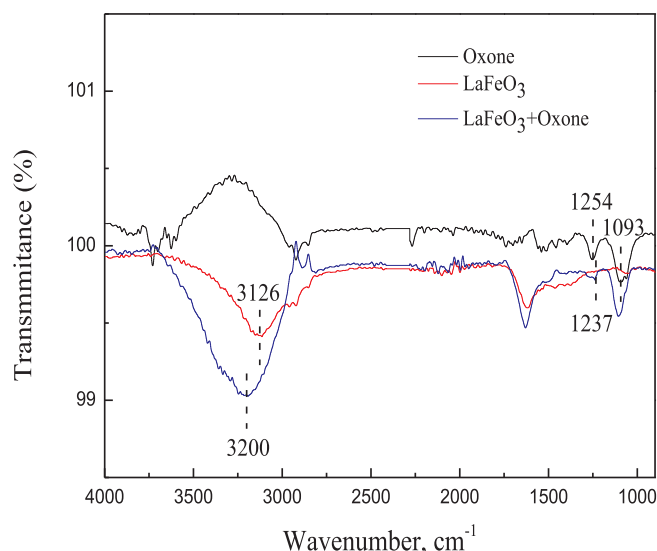
Fig. 7. ATR-FTIR spectra of the sole-PMS solution, LFO particles in water, and LFO particles in PMS solution. (Notes: initial pH of pure water was 7.0, initial pH of the PMS solution was adjusted to pH 7.0).

Fig. 6. (a) H_2-TPR patterns and (b) O_2-TPD of LaFeO$_3$ and Fe$_2$O$_3$.

detect DCF degradation intermediates. Molecular structures were proposed for each intermediate/product based on the molecular ion masses, MS fragment patterns and the isotopic distribution characteristics of chlorine atoms. In total, 15 intermediates/products were detected during DCF degradation by LFO/PMS process. Five intermediates (Compounds 1–5) were identified by SPME/GC/MS while six intermediates (Compounds 5–11) were detected by UPLC/ESI-MS (See Table S1). Compound 5 was detected by both methods. Four low molecular weight acids were identified by IC through comparing their retention time with the standards.

The isotopic distribution of ^{35}Cl and ^{37}Cl satisfies the ratio 3:1 [59], which favors the identification of the degradation intermediates/products of DCF. The intensity of molecular ion peaks of nine intermediates show the isotopic distribution at M/M + 2/M + 4 (9:6:1), indicating all these nine intermediates have two chlorine atoms in their molecular structure. Compounds 6 and 11 are believed to be chlorine-free. The MS of compound 1 show a strong peak at *m/z* 161 with several fragment ion peaks at *m/z* 126 (a chlorine loss) and 90 (two chlorines loss).

Compound 1 can be identified as 2, 6-dichloroaniline, which was corroborated by comparing its retention time and MS patterns with that of the genuine compound. The compound 2 with an accurate mass *m/z* of 202.87 fits the formula $C_8H_7NOCl_2$. The fragment *m/z* 167.91 of compound 2 can be ascribed to a chlorine loss (-35) compared with *m/z* 202.87. The fragment *m/z* 133.01 is believed to come from a further chlorine loss (-35) compared with *m/z* 167.91. Compound 3 presented an exact mass *m/z* of 250.98 which gave the best-fit formula $C_{13}H_{11}NCl_2$. The fragment *m/z* 216.01 of compound 3 derived from a chlorine loss (-35) compared with *m/z* 250.98. The fragment *m/z* 181.05 resulted from a further chlorine loss (-35) compared with *m/z* 216.01. The fragment *m/z* 166.07 can be attributed to a methyl loss (-15) of the fragment *m/z* 181.05. Compound 4 with an accurate mass *m/z* of 264.97 best fit the formula of $C_{13}H_{11}NCl_2$. A chlorine loss of *m/z* 264.97 generated the fragment *m/z* 229.99. The fragment *m/z* 229.99 suffered mass loss of 28 Da (–CO) to generate the fragment *m/z* 202.01 which lost a chlorine, leading to the generation of fragment *m/z* 167.04. Compound 5 suffered a chlorine loss, –CO loss and a further chlorine loss, consequently, leading to the generation of the fragments *m/z* 242.00, 214.00 and 179.04, respectively. Compound 5 was also detected by UPLC/TOF-MS with a fragment *m/z* 250.0136 which came from –CO loss of *m/z* 278.0128. Compounds 7, 8 and 9 which yielded accurate mass *m/z* 312.0187, 282.0084 and 310.0017, respectively, fit the formula of $C_{14}H_{12}NO_3Cl_2$, $C_{13}H_{10}NO_2Cl_2$ and $C_{14}H_{10}NO_3Cl_2$, correspondingly. The experimental mass (*m/z*) of compounds 7, 8 and 9 quite match the calculated mass (*m/z*) of $C_{14}H_{12}NO_3Cl_2$, $C_{13}H_{10}NO_2Cl_2$ and $C_{14}H_{10}NO_3Cl_2$ which is 312.0188, 282.0083 and 310.0032 in that order. The fragments *m/z* 294, 276, and 268 came from 18 Da loss (–H$_2$O) of *m/z* 312, further 18 Da loss (–H$_2$O) of the fragment *m/z* 294, and 44 Da loss (–CO$_2$) of *m/z* 312. Compound 7 is believed to be obtained from the hydroxylation of DCF. The benzene ring with the substitute of acetic acid is more electron-rich than the one substituted by two chlorine atoms, leading to it being more susceptible to the electrophilic attack of sulfate radicals or hydroxyl radicals. The amino group is an electron-donating group and acetic acid group is an electron-withdrawing group, indicating the hydroxylation at C-5 is the best choice. It was also reported C-5 of DCF presented relatively large HOMO coefficient [60], implying C-5 is more prone to be attacked by free radicals. For the case of compound 8, the fragments *m/z* 254 and 247 resulted from 28 Da loss (–CO) of compound 8 (*m/z* 282.0083) and a chlorine loss (-35) of compound 8. Compound 10 may arise from the

further hydroxylation of compound 7. Based on the isotopic distribution of m/z 242, compound 6 is believed to be chlorine-free. Compound 11 derived from compound 6, whose benzene ring was substituted by HO_3SO^- due to the attack of sulfate radical. This was also reported in previous studies [22,61].

Based on the comparison between the retention time of the products and the standards, the peaks at 3.660, 3.967, 4.807 and 7.457 min can be ascribed to lactic acid, acetic acid, formic acid and malonic acid, respectively (See Fig. S10). The peak at 8.957 min is believed to come from sulfate ions. The detailed information of all intermediates/products was described in Table S1.

Fig. 8 illustrates the possible decay pathways of DCF in LFO/PMS system. Four primary intermediates (Compound 1, 3, 5 and 7) were produced at the first stage. The attack of sulfate radical or hydroxyl radical at the *ipso*-position of the imino group led to the cleavage of the C–N bond, forming compound 1. The decarboxylation of DCF gave rise to compound 3. Compound 7 derived from the hydroxylation of DCF owing to the attack of sulfate radicals or hydroxyl radicals at the C-5 site. The ring closure reaction of DCF resulted in the formation of compound 5. It is well documented that ammonia or primary amines can attack aldehydes or ketones to generate imines [62]. In the case of DCF, the nitrogen on the imino group attacks the ketone to form compound 5 with the concomitant loss of H_2O, as shown in Eq. (6).
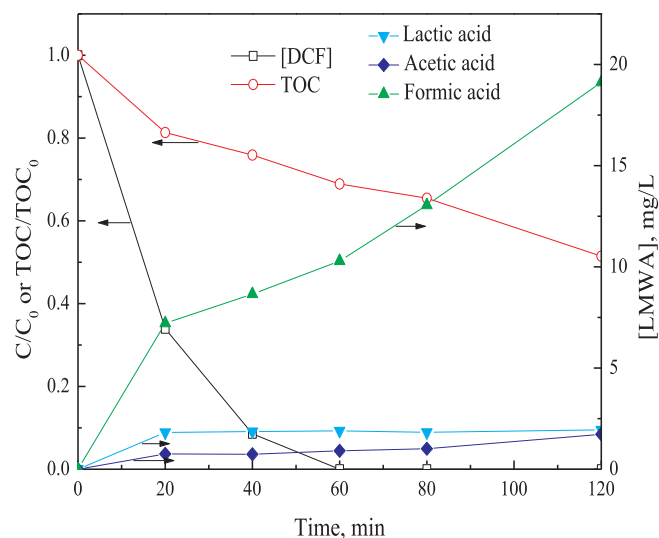

Fig. 9. The evolution profiles of DCF, TOC and low molecular weight acids ($[DCF]_0 = 0.15$ mM, LFO dosage = 0.6 g/L, $[PMS]_0 = 0.3$ mM, tetraborate buffered pH 7.0).
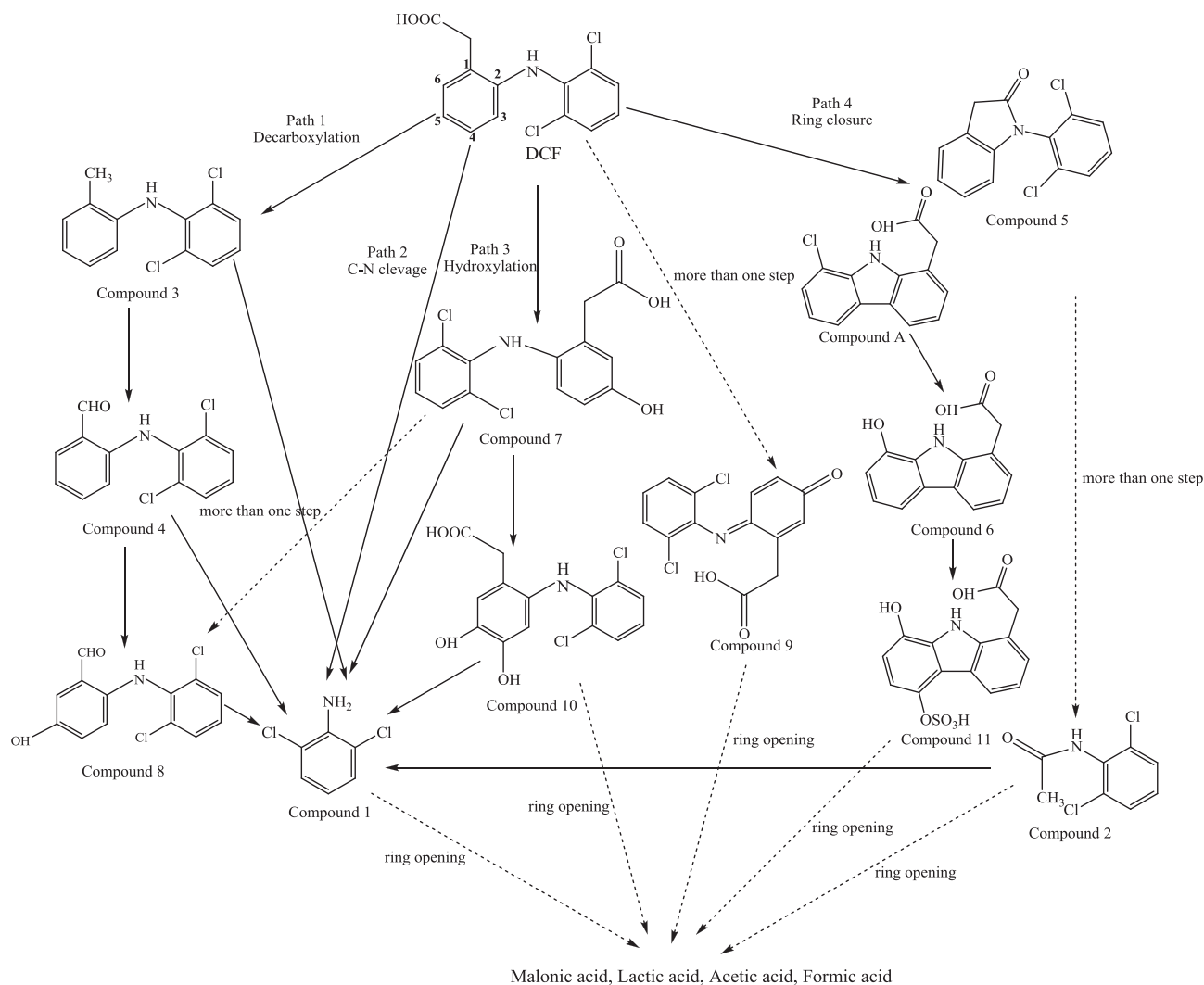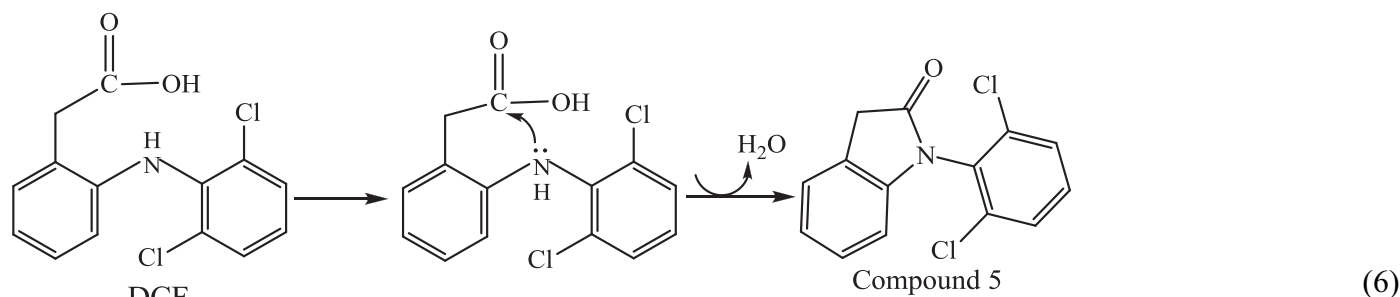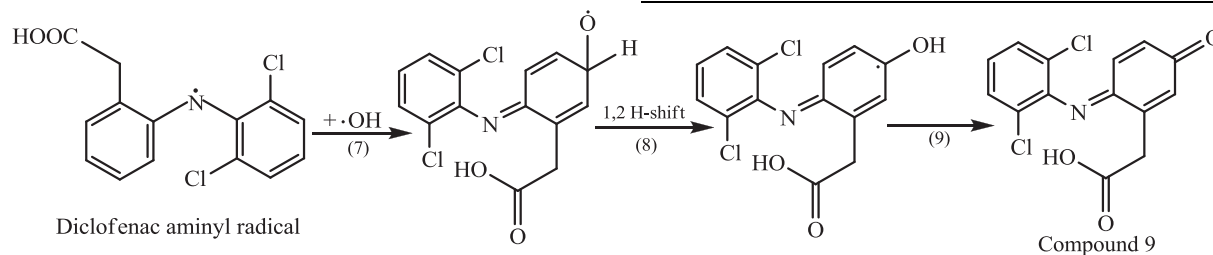

Fig. 8. Possible decay pathways of DCF.

DCF   →   →   Compound 5   (6)

The further oxidation of methyl at the C-1 site of compound 3 resulted in the generation of compound 4. The dechlorination and further intramolecular reaction of DCF could generate compound A via a ring closure. Compound A was not detected in this study. It was detected during DCF degradation by photocatalytic process in a previous study [63]. Compound 6 derived from the dechlorination and hydroxylation of compound A. The benzene ring substituted by HO_3SO^- led to the generation of compound 11. Compound 8 resulted from the hydroxylation of compound 4.

In the case of compound 7, the transformation process may follow three possible ways: (1) the hydroxylation at C-4 site yielded compound 10; (2) the attack of sulfate radical or hydroxyl radical at C-2 site led to the cleavage of C–N bond with the concomitant generation of compound 1; (3) the decarboxylation and further oxidation of methyl at C-1 could also produce compound 8.

The generation of compound 9 may proceed via several steps: (1) the attack of OH on the nitrogen formed diclofenac aminyl radical; (2) the aminyl radical reacts with hydroxyl radical at the C-5 site. A 1, 2-H shift generated a hydroxylcyclohexadienyl radical; (3) The subsequent oxidation of hydroxylcyclohexadienyl radical the led to the formation of compound 9 (diclofenac-2,5-iminoquinone), as described in Eqs. (7–9).

to the formation of inner-sphere complexation between Fe (III) and HSO_5^- and the electron transfer from HSO_5^- to Fe (III). In comparison with Fe_2O_3, it is easier for Fe (III) in LFO structure to be reduced to Fe (II). The presence of abundant oxygen vacancies could encourage the bonding of LFO with PMS. Fifteen oxidation intermediates and products during DCF degradation were identified. The degradation of DCF was believed to involve decarboxylation, dechlorination, C–N cleavage, hydroxylation, intramolecular ring closure and benzene ring opening.

Acknowledgements

Appendix A. Supplementary data

Supplementary data associated with this article can be found, in the online version, at https://doi.org/10.1016/j.cej.2018.07.062.

Diclofenac aminyl radical   + ·OH (7)   1,2 H-shift (8)   (9)   Compound 9

Compound 2 may derive from the ring opening of compound 5. The loss of acetyl group of compound 5 can also yield compound 1. Compound 1 may also result from the cleavage of C–N bond via the attack of sulfate radical or hydroxyl radical at C-1 sites of compounds 3, 4 and 8.

These intermediates suffered ring opening, followed by the generation of various low molecular weight acids. The low molecular weight acids were further oxidized to CO_2 and H_2O. As illustrated in Fig. 9, nearly 50% removal of TOC (initial TOC is around 44.4 mg/L) was achieved after 120 min. The low molecular weight acids contributed to 22.7% of TOC residual, suggesting the benzene rings of some intermediates kept intact after 120 min, which was also confirmed by UPLC-TOF/ESI-MS.

4. Conclusions

A simple and high efficient LFO-activated PMS process was developed in this study. This study provides a deep insight into the mechanism underlying PMS activation by perovskite oxide LFO. Both hydroxyl and sulfate radicals were generated in LFO/PMS system. Sulfate radicals are believed to act as a major player during DCF degradation in this system. The generation of sulfate radicals can mainly be attributed

References

[1] C.G. Daughton, T.A. Ternes, Pharmaceuticals and personal care products in the environment: agents of subtle change? Environ. Health Perspect. 107 (1999) 907–938.
[2] Y.J. Zhang, S.U. Geissen, C. Gal, Carbamazepine and diclofenac: removal in wastewater treatment plants and occurrence in water bodies, Chemosphere 73 (2008) 1151–1161.
[3] R.P. Schwarzenbach, B.I. Escher, K. Fenner, T.B. Hofstetter, C.A. Johnson, U. von Gunten, B. Wehrli, The challenge of micropollutants in aquatic systems, Science 313 (2006) 1072–1077.
[4] M. Chen, J. Yao, Y. Huang, H. Gong, W. Chu, Enhanced photocatalytic degradation of ciprofloxacin over $Bi_2O_3/(BiO)_2CO_3$ heterojunctions: efficiency, kinetics, pathways, mechanisms and toxicity evaluation, Chem. Eng. J. 334 (2018) 453–461.
[5] T.A. Ternes, Occurrence of drugs in German sewage treatment plants and rivers, Water Res. 32 (1998) 3245–3260.
[6] T. Heberer, Occurrence, fate, and removal of pharmaceutical residues in the aquatic environment: a review of recent research data, Toxicol. Lett 131 (2002) 5–17.
[7] F. Groener, C. Hoehne, W. Kleiner, W. Kloas, Chronic diclofenac exposure affects gill integrity and pituitary gene expression and displays estrogenic activity in nile tilapia (Oreochromis niloticus), Chemosphere 166 (2017) 473–481.
[8] J. Schwaiger, H. Ferling, U. Mallow, H. Wintermayr, R.D. Negele, Toxic effects of the non-steroidal anti-inflammatory drug diclofenac Part 1: histopathological alterations and bioaccumulation in rainbow trout, Aquat. Toxicol. 68 (2004) 141–150.
[9] I.C. Guiloski, L.D. Stein Piancini, A.C. Dagostim, S.L. de Morais Calado, L.F. Favaro,

S.L. Boschen, M.M. Cestari, C. da Cunha, H.C. Silva de Assis, Effects of environmentally relevant concentrations of the anti-inflammatory drug diclofenac in freshwater fish Rhamdia quelen, Ecotox. Environ. Safe. 139 (2017) 291–300.

[10] J. Daniel Cardoso-Vera, H. Islas-Flores, N. SanJuan-Reyes, E. Irabella Montero-Castro, M. Galar-Martinez, S. Garcia-Medina, A. Elizalde-Velazquez, O. Dublan-Garcia, L. Manuel Gomez-Olivan, Comparative study of diclofenac-induced embryotoxicity and teratogenesis in Xenopus laevis and Lithobates catesbeianus, using the frog embryo teratogenesis assay: Xenopus (FETAX), Sci. Total Environ. 574 (2017) 467–475.

[11] S. Bae, D. Kim, W. Lee, Degradation of diclofenac by pyrite catalyzed Fenton oxidation, Appl. Catal. B-Environ. 134 (2013) 93–102.

[12] I. Michael, A. Achilleos, D. Lambropoulou, V. Osorio Torrens, S. Perez, M. Petrovic, D. Barcelo, D. Fatta-Kassinos, Proposed transformation pathway and evolution profile of diclofenac and ibuprofen transformation products during (sono)photocatalysis, Appl. Catal. 147 (B-Environ. 2014,) 1015–1027.

[13] H. Yu, E. Nie, J. Xu, S. Yan, W.J. Cooper, W. Song, Degradation of diclofenac by advanced oxidation and reduction processes: kinetic studies, degradation pathways and toxicity assessments, Water Res. 47 (2013) 1909–1918.

[14] M.M. Sein, M. Zedda, J. Tuerk, T.C. Schmidt, A. Golloch, C. von Sonntao, Oxidation of diclofenac with ozone in aqueous solution, Environ. Sci. Technol. 42 (2008) 6656–6662.

[15] V. Naddeo, V. Belgiorno, D. Kassinos, D. Mantzavinos, S. Meric, Ultrasonic degradation, mineralization and detoxification of diclofenac in water: optimization of operating parameters, Ultrason. Sonochem. 17 (2010) 179–185.

[16] X. Cheng, Q. Cheng, X. Deng, P. Wang, H. Liu, A facile and novel strategy to synthesize reduced TiO_2 nanotubes photoelectrode for photoelectrocatalytic degradation of diclofenac, Chemosphere 144 (2016) 888–894.

[17] G.P. Anipsitakis, D.D. Dionysiou, Degradation of organic contaminants in water with sulfate radicals generated by the conjunction of peroxymonosulfate with cobalt, Environ. Sci. Technol. 37 (2003) 4790–4797.

[18] Y.-H. Guan, J. Ma, Y.-M. Ren, Y.-L. Liu, J.-Y. Xiao, L.-Q. Lin, C. Zhang, Efficient degradation of atrazine by magnetic porous copper ferrite catalyzed peroxymonosulfate oxidation via the formation of hydroxyl and sulfate radicals, Water Res. 47 (2013) 5431–5438.

[19] H. Sun, H. Tian, Y. Hardjono, C.E. Buckley, S. Wang, Preparation of cobalt/carbon-xerogel for heterogeneous oxidation of phenol, Catal. Today 186 (2012) 63–68.

[20] H. Liang, Y.Y. Ting, H. Sun, H.M. Ang, M.O. Tade, S. Wang, Solution combustion synthesis of Co oxide-based catalysts for phenol degradation in aqueous solution, J. Colloid Interf. Sci. 372 (2012) 58–62.

[21] F. Qi, W. Chu, B. Xu, Catalytic degradation of caffeine in aqueous solutions by cobalt-MCM41 activation of peroxymonosulfate, Appl. Catal. B-Environ. 134 (2013) 324–332.

[22] X. Pang, Y. Guo, Y. Zhang, B. Xu, F. Qi, $LaCoO_3$ perovskite oxide activation of peroxymonosulfate for aqueous 2-phenyl-5-sulfobenzimidazole degradation: Effect of synthetic method and the reaction mechanism, Chem. Eng. J. 304 (2016) 897–907.

[23] K.-Y.A. Lin, Y.-C. Chen, Y.-F. Lin, $LaMO_3$ perovskites (M = Co, Cu, Fe and Ni) as heterogeneous catalysts for activating peroxymonosulfate in water, Chem. Eng. Sci. 160 (2017) 96–105.

[24] O.P. Taran, A.B. Ayusheev, O.L. Ogorodnikova, I.P. Prosvirin, L.A. Isupova, V.N. Parmon, Perovskite-like catalysts LaBO3 (B = Cu, Fe, Mn Co, Ni) for wet peroxide oxidation of phenol, Appl. Catal. B-Environ. 180 (2016) 86–93.

[25] R.R. Solis, F. Javier Rivas, O. Gimeno, Removal of aqueous metazachlor, tembotrione, tritosulfuron and ethofumesate by heterogeneous monopersulfate decomposition on lanthanum-cobalt perovskites, Appl. Catal. 200 (B-Environ. 2017,) 83–92.

[26] K.-Y.A. Lin, Y.-C. Chen, T.-Y. Lin, H. Yang, Lanthanum cobaltite perovskite supported on zirconia as an efficient heterogeneous catalyst for activating Oxone in water, J. Colloid Interf. Sci. 497 (2017) 325–332.

[27] S. Ben Hammouda, F. Zhao, Z. Safaei, V. Srivastava, D.L. Ramasamy, S. Iftekhar, S. Kalliola, M. Sillanpaa, Degradation and mineralization of phenol in aqueous medium by heterogeneous monopersulfate activation on nanostructured cobalt based-perovskite catalysts ACoO3 (A = La, Ba, Sr and Ce): Characterization, kinetics and mechanism study, Appl. Catal. B-Environ. 215 (2017) 60–73.

[28] Y. Chu, X. Tan, Z. Shen, P. Liu, N. Han, J. Kang, X. Duan, S. Wang, L. Liu, S. Liu, Efficient removal of organic and bacterial pollutants by Ag-La$_{0.8}$Ca$_{0.2}$Fe$_{0.94}$O$_3$-delta perovskite via catalytic peroxymonosulfate activation, J. Hazard. Mater. 356 (2018) 53–60.

[29] X. Duan, C. Su, J. Miao, Y. Zhong, Z. Shao, S. Wang, H. Sun, Insights into perovskite-catalyzed peroxymonosulfate activation: Maneuverable cobalt sites for promoted evolution of sulfate radicals, Appl. Catal. B-Environ. 220 (2018) 626–634.

[30] J. Miao, J. Sunarso, X. Duan, W. Zhou, S. Wang, Z. Shao, Nanostructured Co-Mn containing perovskites for degradation of pollutants: insight into the activity and stability, J. Hazard. Mater. 349 (2018) 177–185.

[31] R.E. Ball, J.O. Edwards, M.L. Haggett, P. Jones, A kinetic and isotopic study of decomposition of monoperoxyphthalic acid, J. Am. Chem. Soc. 89 (1967) 2331–2333.

[32] Y. Rao, D. Xue, H. Pan, J. Feng, Y. Li, Degradation of ibuprofen by a synergistic UV/Fe(III)/Oxone process, Chem. Eng. J. 283 (2016) 65–75.

[33] M.D. Segall, P.J.D. Lindan, M.J. Probert, C.J. Pickard, P.J. Hasnip, S.J. Clark, M.C. Payne, First-principles simulation: ideas, illustrations and the CASTEP code, J. Phys: Condens. Matter 14 (2002) 2717–2744.

[34] Q. Zhang, Y. Huang, S. Peng, Y. Zhang, Z. Shen, J.-J. Cao, W. Ho, S.C. Lee, D.Y.H. Pui, Perovskite LaFeO3-SrTiO3 composite for synergistically enhanced NO removal under visible light excitation, Appl. Catal. B-Environ. 204 (2017) 346–357.

[35] Y. Huang, D. Zhu, Q. Zhang, Y. Zhang, J.-J. Cao, Z. Shen, W. Ho, S.C. Lee, Synthesis

[36] of a $Bi_2O_2CO_3/ZnFe_2O_4$ heterojunction with enhanced photocatalytic activity for visible light irradiation-induced NO removal, Appl. Catal. B-Environ. 234 (2018) 70–78.

[36] Y. Huang, Y. Gao, Q. Zhang, Y. Zhang, J.-J. Cao, W. Ho, S.C. Lee, Biocompatible FeOOH-Carbon quantum dots nanocomposites for gaseous NOx removal under visible light: Improved charge separation and High selectivity, J. Hazard. Mater. 354 (2018) 54–62.

[37] W. Stumm, Chemistry of the Solid-Water Interface: Process at the Mineral-Water and Particle-Water Interface in Natural Systems, John Wiley & Sons, New York, 1992.

[38] T. Zhang, H. Zhu, J.-P. Croue, Production of sulfate radical from peroxymonosulfate induced by a magnetically separable CuFe$_2$O$_4$ spinel in water: efficiency, stability, and mechanism, Environ. Sci. Technol. 47 (2013) 2784–2791.

[39] Y. Xu, J. Ai, H. Zhang, The mechanism of degradation of bisphenol A using the magnetically separable CuFe$_2$O$_4$/peroxymonosulfate heterogeneous oxidation process, J. Hazard. Mater. 309 (2016) 87–96.

[40] R.E. Huie, R.E. Huie, A.B. Ross, Rate constants for reactions of inorganic radicals in aqueous solution, J. Phys. Chem. Ref. Data 17 (1988) 1027–1284.

[41] G.V. Buxton, C.L. Greenstock, W.P. Helman, A.B. Ross, Critical Review of rate constants for reactions of hydrated electrons, hydrogen atoms and hydroxyl radicals (OH/O−) in Aqueous Solution, J. Phys. Chem. Ref. Data 17 (1988) 513–886.

[42] Z.H. Zuo, Z.L. Cai, Y. Katsumura, N. Chitose, Y. Muroya, Reinvestigation of the acid-base equilibrium of the (bi)carbonate radical and pH dependence of its reactivity with inorganic reactants, Radiat. Phys. Chem. 55 (1999) 15–23.

[43] J.R. Bargar, J.D. Kubicki, R. Reitmeyer, J.A. Davis, ATR-FTIR spectroscopic characterization of coexisting carbonate surface complexes on hematite, Geochim. Cosmochim. Acta 69 (2005) 1527–1542.

[44] P. Neta, V. Madhavan, H. Zemel, R.W. Fessenden, Rate constants and mechanism of reaction of sulfate radical anion with aromatic compounds, J. Am. Chem. Soc. 99 (1977) 163–164.

[45] G. Zhao, Y. Zhang, Y. Lei, B. Lv, J. Gao, Y. Zhang, D. Li, Fabrication and electrochemical treatment application of A novel lead dioxide anode with superhydrophobic surfaces, high oxygen evolution potential, and oxidation capability, Environ. Sci. Technol. 44 (2010) 1754–1759.

[46] J. Rivas, R.R. Solis, O. Gimeno, J. Sagasti, Photocatalytic elimination of aqueous 2-methyl-4-chlorophenoxyacetic acid in the presence of commercial and nitrogen-doped TiO$_2$, Int. J. Environ. Sci. Technol. 12 (2015) 513–526.

[47] Z. Wei, F.A. Villamena, L.K. Weavers, Kinetics and mechanism of ultrasonic activation of persulfate: an in Situ EPR spin trapping study, Environ. Sci. Technol. 51 (2017) 3410–3417.

[48] G.S. Timmins, K.J. Liu, E.J.H. Bechara, Y. Kotake, H.M. Swartz, Trapping of free radicals with direct in vivo EPR detection: a comparison of 5,5-dimethyl-1-pyrro-line-N-oxide and 5-diethoxyphosphoryl-5-methyl-1-pyrroline-N-oxide as spin traps for HO$^.$ and SO$_4^.$, Free Radic. Biol. Med. 27 (1999) 329–333.

[49] P. Sabatier, Announcement. Hydrogenation and dehydrogenation for catalysis, Ber. Dtsch. Chem. Ges. 44 (1911) 1984–2001.

[50] K. Li, M. Haneda, Z. Gu, H. Wang, M. Ozawa, Modification of CeO$_2$ on the redox property of Fe$_2$O$_3$, Mater. Lett. 93 (2013) 129–132.

[51] Y. Li, Y. Wan, Y. Li, S. Zhan, Q. Guan, Y. Tian, Low-temperature selective catalytic reduction of NO with NH$_3$ over Mn$_2$O$_3$-Doped Fe$_2$O$_3$ hexagonal microsheets, Acs Appl. Mater. Inter. 8 (2016) 5224–5233.

[52] K. Ji, H. Dai, J. Deng, L. Song, S. Xie, W. Han, Glucose-assisted hydrothermal preparation and catalytic performance of porous LaFeO$_3$ for toluene combustion, J. Solid State Chem. 199 (2013) 164–170.

[53] Z. Zhao, X.G. Yang, Y. Wu, Comparative study of Nickel-based perovskite-like mixed oxide catalysts for direct decomposition of NO, Appl. Catal. B-Environ. 8 (1996) 281–297.

[54] G. Pecchi, M.G. Jiliberto, A. Buljan, E.J. Delgado, Relation between defects and catalytic activity of calcium doped LaFeO$_3$ perovskite, Solid State Ionics 187 (2011) 27–32.

[55] R. You, Y. Zhang, D. Liu, M. Meng, Z. Jiang, S. Zhang, Y. Huang, A series of ceria supported lean-burn NOx trap catalysts LaCoO$_3$/K$_2$CO$_3$/CeO$_2$ using perovskite as active component, Chem. Eng. J. 260 (2015) 357–367.

[56] C. Su, X. Duan, J. Miao, Y. Zhong, W. Zhou, S. Wang, Z. Shao, Mixed conducting perovskite materials as superior catalysts for fast aqueous-phase advanced oxidation: a mechanistic study, Acs Catal. 7 (2017) 388–397.

[57] G.P. Anipsitakis, D.D. Dionysiou, Radical generation by the interaction of transition metals with common oxidants, Environ. Sci. Technol. 38 (2004) 3705–3712.

[58] J. Gonzalez, M. Torrent-Sucarrat, J.M. Anglada, The reactions of SO$_3$ with HO$_2$ radical and H$_2$O center dot center dot center dot HO$_2$ radical complex. Theoretical study on the atmospheric formation of HSO$_5$ and H$_2$SO$_4$, Phys. Chem. Chem. Phys. 12 (2010) 2116–2125.

[59] H. Cheng, D. Song, H. Liu, J. Qu, Permanganate oxidation of diclofenac: The pH-dependent reaction kinetics and a ring-opening mechanism, Chemosphere 136 (2015) 297–304.

[60] D. Vogna, R. Marotta, A. Napolitano, R. Andreozzi, M. d'Ischia, Advanced oxidation of the pharmaceutical drug diclofenac with UV/H$_2$O$_2$ and ozone, Water Res. 38 (2004) 414–422.

[61] L.J. Xu, W. Chu, L. Gan, Environmental application of graphene-based CoFe$_2$O$_4$ as an activator of peroxymonosulfate for the degradation of a plasticizer, Chem. Eng. J. 263 (2015) 435–443.

[62] K. Peter, S. Voldhardt, N.E. Schore, Organic Chemistry, W.H. Freeman & Co, New York, 1987.

[63] C. Martinez, M. Canle, M.I. Fernandez, J.A. Santaballa, J. Faria, Aqueous degradation of diclofenac by heterogeneous photocatalysis using nanostructured materials, Appl. Catal. B-Environ. 107 (2011) 110–118.